A new and effective method for thermostatting confined fluids

Sergio De Luca,[1] B. D. Todd,[1,a)] J. S. Hansen,[2] and Peter J. Daivis[3]
[1]*Department of Mathematics, Faculty of Science, Engineering and Technology, and Centre for Molecular Simulation, Swinburne University of Technology, Melbourne, Victoria 3122, Australia*
[2]*DNRF Center "Glass and Time," IMFUFA, Department of Science, Systems and Models, Roskilde University, DK-4000 Roskilde, Denmark*
[3]*School of Applied Sciences, RMIT University, Melbourne, Victoria 3001, Australia*

(Received 7 October 2013; accepted 23 December 2013; published online 3 February 2014)

We present a simple thermostatting method suitable for nanoconfined fluid systems. Two conventional strategies involve thermostatting the fluid directly or employing a thermal wall that couples only the wall atoms with the thermostat. When only a thermal wall is implemented, the temperature control of the fluid is true to the actual experiment and the heat is transferred from the fluid to the walls. However, for large or complex systems it can often be computationally prohibitive to employ thermal walls. To overcome this limitation many researchers choose to freeze wall atoms and instead apply a synthetic thermostat to the fluid directly through the equations of motion. This, however, can have serious consequences for the mechanical, thermodynamic, and dynamical properties of the fluid by introducing unphysical behaviour into the system [Bernardi *et al.*, J. Chem. Phys. **132**, 244706 (2010)]. In this paper, we propose a simple scheme which enables working with both frozen walls and naturally thermostatted liquids. This is done by superimposing the walls with oscillating particles, which vibrate on the edge of the fluid control volume. These particles exchange energy with the fluid molecules, but do not interact with wall atoms or each other, thus behaving as virtual particles. Their displacements violate the Lindemann criterion for melting, in such a way that the net effect would not amount to an additional confining surface. One advantage over standard techniques is the reduced computational cost, particularly for large walls, since they can be kept rigid. Another advantage over accepted strategies is the opportunity to freeze complex charged walls such as β-cristobalite. The method furthermore overcomes the problem with polar fluids such as water, as thermalized charged surfaces require higher spring constants to preserve structural stability, due to the effects of strong Coulomb interactions, thus inevitably degrading the thermostatting efficiency.
 [http://dx.doi.org/10.1063/1.4862544]

I. INTRODUCTION

In the last decade, nonequilibrium molecular dynamics (NEMD) of confined fluids has seen rapid growth, to the extent that it is now regarded as an essential tool to study liquid transport at the nanoscale.[1] Typically, flow production is achieved by the action of external gravity-like forces,[2–4] or shear forces exerted by moving wall boundaries,[5–7] yielding classical Poiseuille and Couette flow profiles, respectively. Flows of liquids with diluted ions can be sustained by the action of electric fields, as in electro-osmotic flow.[8] The external perturbation drives the fluid out of equilibrium, performing work and heats up the system. To attain steady state, the excess heat must be removed from the system. When no work is performed by external agents, for instance, when structural and diffusion properties of water near interfaces are the focus,[9] a thermostat is required to fix the thermodynamic state point of the fluid. Several options are at one's disposal, such as the Berendsen,[10] Langevin,[11] Gaussian isokinetic,[12] Andersen,[13] configurational,[14,15] and the Nosé-Hoover thermostats.[16–18] Of these the latter is renowned for its ability to sample the canonical ensemble at equilibrium.[18] Details of these thermostats can be found in a number of molecular dynamics textbooks.[12,19–23]

Several classes of materials and geometries are employed as surfaces to which fluids are confined. Graphene surfaces and carbon nanotubes[24] are remarkable examples for their potential applications in nanofluidics, such as chemical sensors,[25] microelectronics,[26] and desalination membranes.[27] Alternatively, simpler arrangements such as the BCC (body-centered-cubic) or FCC (face-centered-cubic) crystal structures are widely used in molecular dynamics simulation modeling of metal surfaces or simple container templates. These structures may be fixed in space, or subjected to rigid translation to shear the fluid. Since rigid structures cannot transport heat, the fluid must be directly thermostatted to reach the steady state. In confined fluid NEMD simulations, it is often considered appropriate to thermostat only in the directions perpendicular to the fluid velocity,[28,29] to reduce interferences in the flow direction. However, the PUT thermostat[30,31] (Profile Unbiased Thermostat) makes it possible to correctly thermostat also in the direction of the flow by subtracting the streaming velocity contribution. Alternatively, thermal walls can be implemented. Surface atoms are modelled with particles oscillating around their equilibrium lattice positions,[32] and the heat is transported

a)btodd@swin.edu.au

across the fluid and into the walls, resembling a real experiment.

It has been pointed out that for boundary driven Couette flow,[33,34] thermostatting the fluid may be unrealistic since it eliminates all temperature gradients and heat fluxes. Removing the heat from the fluid at a rate which is higher than the natural conduction through walls may result in highly nonphysical situations.[33] The heat dissipated does not naturally redistribute between all the degrees of freedom, which could manifest itself in an unrealistic steady state and incorrect values at nonlinear transport properties such as the first normal stress coefficient.[35,36]

Recently, Bernardi *et al.*[37] investigated how distinct thermostatting techniques may affect diverse mechanical properties of nanoconfined fluids such as velocity, density, temperature and shear stresses. Under Couette flow, a comparison was made between the direct application of a thermostat on the fluid, and the thermal wall strategy. Results were complemented with an analysis of the Lyapunov spectra, which reveals the chaotic dynamics near the interfaces. They found unphysical temperature profiles, inconsistent streaming velocity profiles and stronger density profile fluctuations when the walls were rigid and the fluid was thermostatted. The Lyapunov analysis confirmed that thermostatting the fluid biases the dynamics near the interfaces. They concluded that the best agreement with hydrodynamic predictions is attainable if only the walls are thermostatted. Yong and Zhang[38] applied different thermostatting algorithms to the wall only, to the wall and the fluid, and only to the fluid, under the same Couette flow geometry. They found that thermostatting the fluid in strongly sheared systems may give unphysical results. Further studies[5,31,39] demonstrated that coupling the fluid with a thermostat may affect the properties of molecularly structured fluids, inducing unwanted average torques on molecules and affecting their orientational ordering.

In any situation where the heat transfer at the fluid-solid interfaces must be realistic, thermal walls may be the only reliable method. A typical thermal wall is made of atoms tethered to lattice sites with springs imparting oscillations to the atoms, frequently arranged as FCC or BCC crystal structures, and bonded to their equilibrium lattice positions $\mathbf{r}_{i0}$ by the force

$$\mathbf{F}_{e,i} = -k(\mathbf{r}_i - \mathbf{r}_{i0}), \tag{1}$$

where k is the wall spring constant, and $\mathbf{r}_i$ represents the vector position of a wall particle. Realistic implementations require that the mean-square displacement of the wall atoms do not exceed the Lindemann criterion for melting[40]

$$\frac{\langle|\mathbf{r}_i - \mathbf{r}_{i0}|^2\rangle^{1/2}}{d_{min}} < 0.15 \tag{2}$$

in which $\langle|\mathbf{r}_i - \mathbf{r}_{i0}|^2\rangle$ is the mean-square displacement of the wall atoms from their equilibrium position and d_{min} is the smallest distance between nearest neighbors of the solid under investigation. The spring stiffness should preserve the solid state structure during the course of the simulations to prevent liquid atoms from penetrating the walls.

When the temperatures are very high, the walls may not sustain the pressure exerted by the liquid, which may permeate or disrupt the surface. Tuning the stiffness of the spring may solve this complication. In some circumstances, softer wall springs are required to properly thermostat the fluid, and to recover stability an additional barrier wall may be inserted close to the surface.[41] To enhance stability, wall particles may be made to interact between themselves. However, with N wall atoms the computational cost may scale as N^2 or $N\log N$ when implementing the neighbor list method in conjunction with a linked list,[21] which can be expensive for larger or complex walls. The computational cost is even larger when the stability of the carbon structure is maintained by three-body interaction potentials such as the Brenner potential.[42] A recent interactive thermal wall model was devised in the context of two-dimensional shear-driven flow of liquid argon,[43] and three-dimensional systems,[44] which scales as N and allows complex treatment of the thermal boundary condition at interfaces. Other advanced thermal wall models are the phantom method,[45–47] in which a layer of additional molecules is placed below the real wall and connected with the real particles with special springs, mimiking the infinitely wide bulk solid, and the variable boundary temperature method[48] (VBT), which accurately models the thermal conduction inside the wall. Extensive reviews and critical discussions of different aspects of thermal walls, including schemes which do not involve elastic spring forces, can be found in the literature,[43,49,50] and many references therein.

In the framework of thermal walls, when complex, charged crystal structures confine polar fluids, a spring constant value which imparts stability, simultaneously enabling efficient heat transport through the walls, may be difficult to obtain. We have verified[51] that when the plane (111) of β-cristobalite,[52–56] with silanol surface density $\sigma = 4.55$(SiOH) /nm^2,[57] is exposed to SPC/E[58,59] water molecules embedded in an electric field of the order $\approx$1 VÅ^{-1},[60] the values of k satisfying Eq. (2) lead to atomic vibrational frequencies which degrade the thermostatting performance. A Nosé-Hoover thermostat fixing $T_{wall} = 300$ K was used. Softening the spring stiffness improves the thermostatting performance, but water may permeate the wall. Allowing wall interparticle interactions mitigates the difficulty. However, the tethrahedral and surface atomic arrangement of (111) β-cristobalite implies more than one interatomic distance separation, which makes stabilizing the repulsive interactions with a single σ Lennard-Jones[20] parameter very difficult. Hence, working with a rigid wall may solve the problem, but this would make it mandatory to thermostat the fluid directly.

To overcome these difficulties we have devised a simple scheme which enables rigid walls to coexist with unthermostatted fluids. This solves the stability issues discussed above, impeding penetration of liquid molecules through the surfaces, and circumventing any thermostat interference on the fluid dynamics. Moreover, using a rigid wall together with so-called "virtual particles" is much more computationally efficient than fully vibrating walls, especially if the wall is dense and multilayered. The reason, which will be detailed in Sec. II, is that the number of virtual particles does not depend on the characteristics of the rigid wall and can be much less than the number of atoms composing the real surface. Finally, the method preserves the natural temperature profiles in

fluids. As will be explained, the displacements of the virtual wall particles violate the Lindemann criterion for melting. To demonstrate our scheme we utilize two graphene layers rather than two (111) β-cristobalite slabs, whose strong hydrophilicity and adsorption characteristics[61–65] would have concealed some features of the model.

We describe our virtual particle thermostatting procedure (VP scheme) in the context of Poiseuille flow, making comparison with the thermal wall approach, in which the Nosé-Hoover thermostat is applied to wall particles (TW scheme). We investigate mechanical properties like the streaming velocity, density and temperature profiles, for different gravity-like forces and varying the parameters at our disposal. To further validate the method, we quantify the heat flux and the Kapitza resistance[66,67] at the solid-liquid interface, making comparison with molecular dynamics (MD) and experimental values taken from the literature.

II. THERMOSTAT DESIGN AND SIMULATIONS

We performed NEMD simulations with code developed by the authors. The system under investigation includes two planar surfaces confining $N = 314$ water molecules. Water was modeled with the SPC/E pair potential.[58] The partial charges of the SPC/E model are $q_{\mathrm{H}} = 0.4238e$ and $q_{\mathrm{O}} = -0.8476e$ for hydrogen and oxygen, respectively ($e = 1.6 \times 10^{-19}$ C is the fundamental unit of charge). The SHAKE algorithm[68] was implemented to maintain the rigid structure of the water molecule, with the O–H bond length fixed at 0.1 nm and the H–O–H angle fixed at 109.5°. The resulting structure yields a dipole moment of 2.35 D, within uncertainties of the experimental value of 2.9 ± 0.6 D.[69] The rectangular simulation box has dimensions $L_x = 1.969$ nm, $L_y = 6.368$ nm, and $L_z = 2.131$ nm, and is periodic in the x and z directions (the fluid is confined in the y direction).

Solid graphene[70–72] wall surfaces were modeled with a monolayer of carbon atoms arranged in a hexagonal lattice with bond length 0.142 nm. Its mechanical properties make it an excellent container for fluid transport purposes. Two graphene layers are parallel to the $x - z$ planes, with center of mass separation $h = 2.57$ nm. The Lennard-Jones interaction potential parameters between the oxygen of the water and the carbon atoms are $\epsilon_{\mathrm{CO}} = 0.392$ kJ/mol and $\sigma_{\mathrm{CO}} = 0.319$ nm,[73] with $\sigma_{\mathrm{CH}} = 0$ and $\epsilon_{\mathrm{CH}} = 0$ since the hydrogen of water does not interact with the carbon atoms. We neglect polarizability effects of the water/graphene interface.[74]

When under the action of shear, pressure or electric driving forces, the friction between molecules produces heat which must be removed by a thermostat. Consider a rectangular grid of oscillating virtual particles, with their equilibrium positions distributed, at the beginning of the simulation, on a plane parallel to the $x - z$ direction (VP plane), placed close to the fixed, graphene layer. Their task is only to absorb heat from the water. They thus only interact with water molecules, are allowed to oscillate only in the y direction, do not interact with the graphene wall atoms and do not interact between themselves. In a standard vibrating wall, the mean-square displacement of the atoms with respect to their equilibrium position is very small, typically a fraction of the interatomic lattice site distances. As explained, this is required to preserve the solid structure of the wall, and is usually achieved by having wall atom oscillation amplitudes which respect the Lindemann criterion for melting, Eq. (2). Selecting suitable values for the wall spring constant, which is the main parameter that determines the amplitude and frequency of the oscillations,[75] the stiffness of the wall atoms can be tuned such that their dynamics evolve in accord with the Lindemann criterion. The oscillation amplitudes are mainly governed by the stiffness k and the frequency is proportional to $\sqrt{k/m}$, where m is the mass of the wall atom.[76]

Contrary to the standard case, in our scheme the VP plane should *not* behave like a solid wall. In other words, water molecules should not interact with the virtual particles as a rigid barrier. To achieve this, the amplitudes of the VP harmonic motion do not respect the Lindemann criterion for melting, that is, the root mean-square displacement of the VP i located at the instantaneous position $r_{i,\,y}$ (with equilibrium position $r_{i0,\,y}$) should satisfy $\langle |r_{i,\,y} - r_{i0,\,y}|^2 \rangle^{1/2} > 0.15 \times d_{min}$. The inequality may be satisfied using low values for the spring constant, which typically would not keep the solid state of a standard thermal wall. For instance, in the case of graphene, assuming $d_{min} = 0.142$ nm, we obtain $|r_{i,\,y} - r_{i0,\,y}| > 0.21$ Å. The requirement can be achieved with spring constant values of the order $k \approx 0.5$ Nm^{-1}. With $k \approx 0.5$ Nm^{-1} at $T = 298$ K we observe $|r_{i,\,y} - r_{i0,\,y}| \approx 3$ Å from the VP plane to empty space (opposite to the fluid volume), during simulations. Note that we set the mass of a VP equal to the mass of oxygen. To further enforce this characteristic, we do not constrain the center of mass momentum of the VP plane particles, which would amount to an extra pressure on the fluid volume, screening the natural water-graphene interactions. We point out that lower spring constants correspond to lower wall atom oscillation frequencies,[75] enabling the use of larger MD time steps. In the outlined setting, the $x - z$ coordinates of the VP may be identified as local heat absorbers, virtually attaching thermal transport attributes to the rigid wall.

The VP temperature is fixed at $T_{VP} = 298$ K, by rescaling the kinetic energy. At every time step the amount of heat removed or transmitted to the VP is

$$\Delta E(t) = \frac{1}{2} \sum_{j=1}^{N} m_j v_j(t)^2 - \frac{D}{2} N k_B T_{VP} \tag{3}$$

which can be done evaluating the instantaneous VP temperature

$$T_{VP}(t) = \sum_{j=1}^{N} m_j v_j(t)^2 / D N k_B \tag{4}$$

and multiplying the VP velocities by the factor $\sqrt{T_{VP}/T_{VP}(t)}$, where $D = 1$ is the translational degree of freedom for the y-direction motion, N is the total number of VP, and k_B is the Boltzmann constant.

We verified that applying the Nosé-Hoover thermostat to the VP, instead of the simpler rescaling procedure, does not significantly affect the results. Note that in the context of thermal walls, any of the thermostatting algorithms mentioned in Sec. I may be applied to the walls, and often a simple velocity rescaling method may be a feasible scheme.[77] Moreover, our

verification is compatible with the findings of Liu and Li[78] who demonstrated, in the same context, that the rescaling approach does not significantly affect the temperature distributions obtained compared to other thermostats that couple with walls.

We designate as d_{gv} the perpendicular separation between the graphene layer and the VP plane. Setting $d_{gv} = 0$ indicates that the VP plane and the graphene layer lie on the same horizontal plane. Choosing $d_{gv} > 0$ implies shifting the VP plane inside the fluid, whereas $d_{gv} < 0$ primarily exposes graphene to water and moves the VP plane inside the graphene walls. A schematic diagram of the system for the three cases is depicted in Fig. 1. Note that in setting d_{gv} we fix (at the beginning of the simulation) the y-coordinate of the VP plane equilibrium position (which does not change). However, during the simulation the average y-coordinate of the VP plane *does* change and may not coincide with the initial equilibrium y-coordinate since the center of mass of the VP plane is not constrained. This is particularly emphasized if $d_{gv} > 0$, a circumstance in which the VP are pushed back by the water.

We distribute on a rectangular grid 36 particles per VP plane, with the x-direction interparticle separation being $\Delta l_x = L_x/6$ and z-direction $\Delta l_z = L_z/6$, arranging one VP plane for each real surface. Each graphene layer is composed of 160 carbon atoms. The interactions between water molecules have been modeled by means of the 12 − 6 Lennard-Jones (LJ) potential and point charge Coulomb interaction between the atoms making up the water molecules

$$\phi_{ij} = \sum_i \sum_{j>i} 4\epsilon_{ij} \left[\left(\frac{\sigma_{ij}}{r_{ij}} \right)^{12} - \left(\frac{\sigma_{ij}}{r_{ij}} \right)^{6} \right] + \sum_i \sum_{j>i} \frac{q_i q_j}{4\pi\epsilon_0 r_{ij}}, \tag{5}$$

where the first term in parenthesis represents the short range repulsive part and the second term models the dipole-induced attractive part. The Coulomb term describes the electric interactions between charged sites of different molecules, computed with the Wolf algorithm[79] with a cut-off truncation radius of 0.918 nm and a damping coefficient $\alpha = 0.06$ Å^{-1}.[80] The Wolf method requires two parameters, the cut-off radius and the damping coefficient. In Ref. 80, it was shown that the structural and dynamical properties were recaptured for liquid water for cut-off of around 9 Å and damping coefficient in the range 0–0.06 Å^{-1} which is what we apply here. It is worth stressing that truncating and shifting the Coulomb force in this manner induces a fictitious electrical field in anisotropic systems such as confined fluids. However, this effect is usually small and will not have effects on the results presented in this paper. The constant ϵ_{ij} which represents the depth of the LJ potential, is employed as an energy scale parameter, while σ_{ij}, the particle distance at which $\phi_{ij} = 0$, is used as a length scale parameter, and $\epsilon_0 = 8.854 \times 10^{-12}$ Fm^{-1} is the vacuum permittivity. For oxygen-oxygen interactions we used the SPC/E Lennard-Jones parameters $\epsilon = 0.6502$ kJ/mol and $\sigma = 0.3166$ nm, and for hydrogen-hydrogen and oxygen-hydrogen they are 0. We fix $\epsilon_{wVP} = \epsilon$ and $\sigma_{wVP} = \sigma$ for the Lennard-Jones interaction between VP and water. The distance between two sites of different molecules is $r_{ij} = |\mathbf{r}_i - \mathbf{r}_j|$, where $\mathbf{r}_i$ and $\mathbf{r}_j$ are the position vectors of the

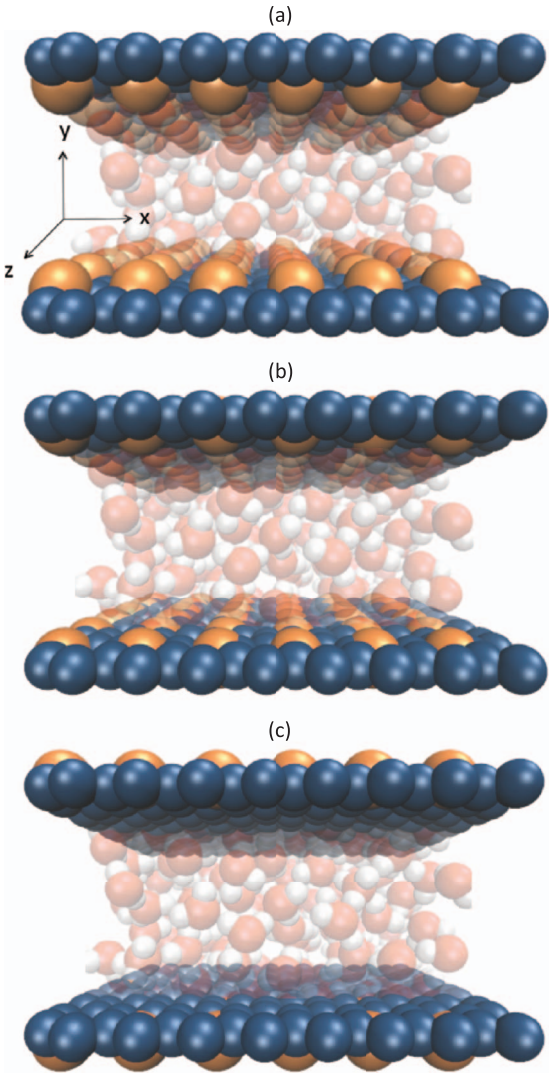

FIG. 1. (a) Schematic of the graphene walls (blue) and the overlapping VP plane particles (yellow) in their initial configuration. The distance between the two layers is $d_{gw} > 0$, (b) $d_{gw} = 0$, (c) $d_{gw} < 0$. Partially transparent water molecules are displayed between the walls.

oxygen and hydrogen sites of water, the graphene atoms and the VP. The mass scaling factor is $m_O = 16$ a.m.u. with VP mass $m_{VP} = m_O$. The water-water, water-graphene and water-VP LJ interaction potential is truncated at $r = 2.5\sigma$ and the force on atom i of a water molecule is

$$\mathbf{F}_i(\mathbf{r}_i) = -\sum_{j\neq i}^{N_{tot}} \frac{\partial \phi_{ij}(\mathbf{r}_{ij})}{\partial \mathbf{r}_i}, \tag{6}$$

where N_{tot} is the total number of atoms in the system. When water molecules interact with the graphene atoms and the VP particles the term ϕ_{ij} represents only the LJ interaction between oxygen and graphene, and oxygen and VP particles, with the LJ parameters explained before. Note that the hydrogen do not LJ interacts with the other atoms and the graphene and VP particles are uncharged.

The Newtonian equations of motion for oxygen and hydrogen with the inclusion of a body force term are

$$\dot{\mathbf{r}}_i = \frac{\mathbf{p}_i}{m_i}, \tag{7}$$

$$\dot{\mathbf{p}}_i = \mathbf{F}_i + m_i \mathbf{g}, \tag{8}$$

where m_i is the mass of atom i, $\mathbf{p}_i$ is the laboratory momentum of atom i, $\mathbf{F}_i$ represents the total intermolecular force acting on atom i due to all other atoms, and $\mathbf{g} = (g, 0, 0)$ is the time-independent external gravity-like field acting on atom i, along the x-direction. The magnitude of the external field g is set such as to attain steady state in the accessible simulation time, whilst simultaneously avoiding excessive heating. The leap-frog integration algorithm[21] is adopted to evolve the Newtonian equations of motion, with a time step $\Delta t = 1.57$ fs. The Newtonian equations of motion for the VP read

$$\dot{\mathbf{r}}_i = \frac{\mathbf{p}_i}{m_{VP,i}}, \tag{9}$$

$$\dot{\mathbf{p}}_i = \mathbf{F}_i + \mathbf{F}_{e,i}, \tag{10}$$

where m_{VP} is the mass of VP, $\mathbf{p}_i$ is its laboratory momentum, $\mathbf{F}_i$ represents the total intermolecular force acting on the virtual particle i due to water molecules and $\mathbf{F}_{e,i}$ represents the spring force acting on the virtual particle, see Eq. (1). In Sec. III we will also make use of the so-called VP-3D scheme, in which the VP oscillation is not constrained in the y-direction, but occurs in the x, y, z directions, as in the atoms of a thermal wall. In this case $D = 3$ in Eqs. (3) and (4).

At the start of each simulation, water molecules are distributed on a grid such that oxygen atoms do not overlap, and the VP are arranged as previously described. The system is allowed to equilibrate for the first 10^5 time steps, after which a further 10^5 time steps were run in order to collect equilibrium density profiles. After this the field was applied to the water molecules. Before accumulating time averages of quantities of interest, we allowed the system to attain steady-state, typically after 5×10^6 time steps. Averages of dynamical quantities were collected by applying standard binning techniques,[20] with 101 bins of size $\Delta y = 0.25$ Å, sampling every 10 time steps.

To compute the streaming velocity $v_x(y)$ we make use of the microscopic definition of the momentum flux density, plotted against the (y-direction) distance between the two graphene surfaces, which corresponds to the y-direction

$$J_x(y, t) = \sum_i m_i v_{x,i} \delta(y - y_i) \tag{11}$$

divided by the mass density:

$$\rho(y, t) = \sum_i m_i \delta(y - y_i), \tag{12}$$

where i indexes molecule i, m_i is the mass of water molecule i, $v_{x,i}$ is the x-velocity component of the ith water molecule averaged over the x and z coordinates and y_i is the y-component center of mass of molecule i. The streaming velocity is averaged on slabs located between y and $y + \Delta y$, where y extends over the range 0–2.57 nm. At the end of the simulation, the streaming velocity is computed for every bin as

$$v_x(y) = \frac{\left\langle \sum_i m_i v_{x,i} \delta(y_i - y) \right\rangle}{\left\langle \sum_i m_i \delta(y_i - y) \right\rangle}, \tag{13}$$

where the angle brackets denote time averages over 7.85 ns.

The liquid temperature depends on the external field, the location of the VP plane and several VP parameters, as will be detailed in Sec. III. We monitor this property by means of the same binning technique explained above, evaluating the molecular centre of mass kinetic temperature

$$T_m = \frac{1}{3Nk_B} \sum_i m_i \mathbf{c}_{i,cm}^2 \tag{14}$$

for every bin, where N is the total number of water molecules accumulated in the particular bin and $\mathbf{c}_{i,cm}$ is the *thermal* velocity of the center of mass of molecule i (i.e., we subtract the contribution of the streaming center of mass velocity, Eq. (13)).

III. RESULTS

We performed NEMD simulations with force magnitudes in the range $F = (1.28 - 6.42) \times 10^{13}$ ms^{-2}. The LJ water-VP parameters (which later on will be individually varied keeping the force fixed at a reference value) are as follows: $\sigma_{wVP} = 0.3166$ nm, $\epsilon_{wVP} = 0.6502$ kJ/mol, $k_{VP} = 0.431$ Nm^{-1}, $d_{gv} = 0.63$ Å, and $N_{VP} = 36$ particles per virtual plane.

Fig. 2 shows streaming velocity profiles for varying fields, with green and red profiles depicting the lowest and highest applied force field, respectively. The velocity slip at the boundary increases as the field strength increases, qualitatively reproducing the fluid slip characteristic behaviour at the solid interface.[81] Moreover, profiles can be fitted with a parabolic curve, hence the Poiseuille flow characteristic shape is preserved.

Fig. 3(a) display temperature profiles for the VP system. These results can be compared with those of Fig. 3(b), in which a classical thermal wall was implemented, coupling the Nosé-Hoover thermostat to the graphene atoms and using the spring constant $k_{TW} = 3.23$ Nm^{-1}. This value

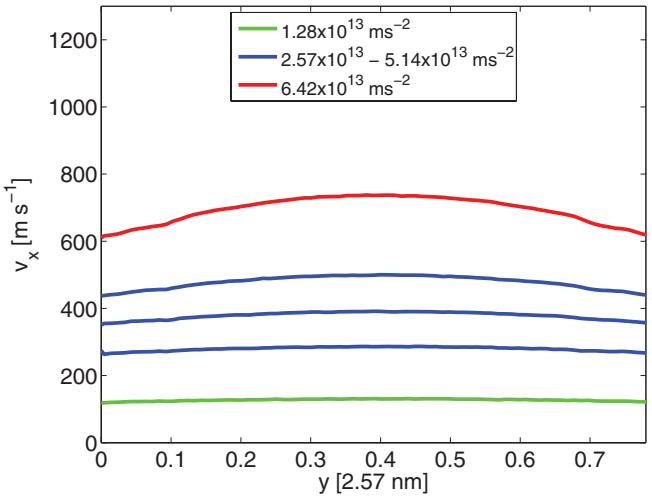

FIG. 2. Streaming velocity profiles of water thermostatted with the VP method. The horizontal axis represents the distance between the walls (subtracting out the depleted region width), measured along the y-coordinate of the simulation box. The five external fields are ordinated in the legend. The horizontal axis represents the width $h' \lesssim h_{eff} \simeq 0.80 \times 2.57$ nm $\simeq 2$ nm.

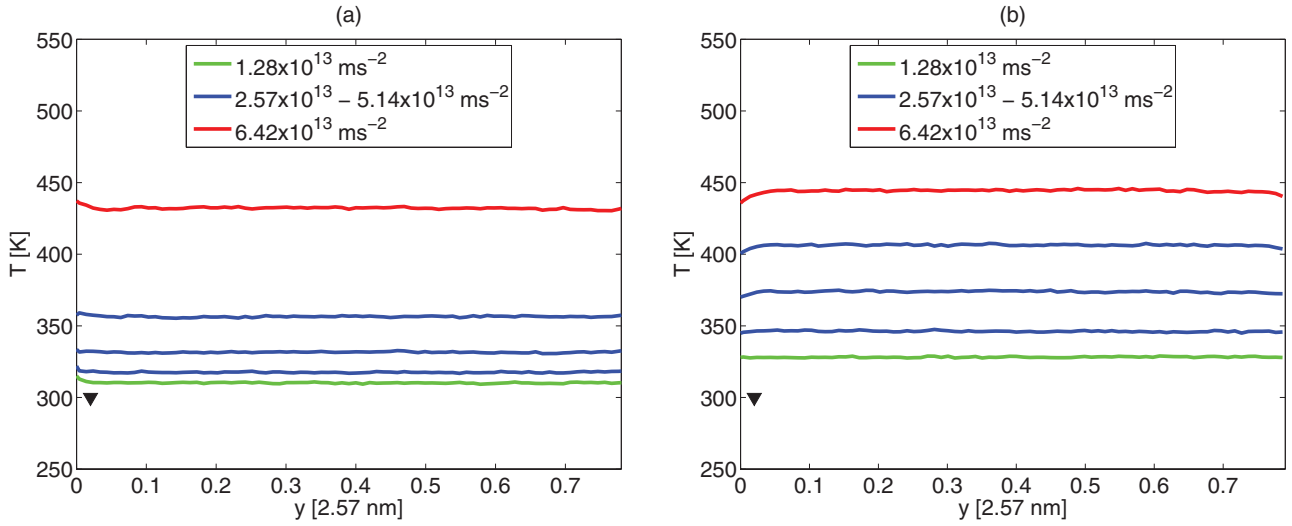

FIG. 3. (a) Temperature profiles of water thermostatted with the VP method and, (b) Thermal wall (TW) scheme. The horizontal axis represents the width $h' \lesssim h_{eff} \simeq 0.80 \times 2.57$ nm $\simeq 2$ nm. The black triangle represents the temperature of the VP thermostat.

was demonstrated to preserve wall stability and maintain the thermostatting functionality.[60] For the reasons explained in Sec. II, the spring constant of the VP should be less than typical values used to preserve the wall solid state. This justifies our choice $k_{TW} \gg k_{VP}$. Note that no VP and no thermostat was applied to the fluid in the TW implementation. It is evident from Fig. 3 that both the VP and TW schemes are able to exhibit temperature discontinuity at the interfaces, due to the Kapitza resistance.[82,83] Fluid temperatures appear similar, ranging in both cases from ~300 K to ~500 K, when the field increases from $F = 1.28 \times 10^{13}$ ms^{-2} to $F = 6.42 \times 10^{13}$ ms^{-2}. Later on we will demonstrate that changing the several VP parameters at our disposal allows us to achieve a wide range of fluid temperatures at fixed field. Moreover, we will show specific sets of VP parameters that enable VP to attain the same thermostatting performance of TW. We emphasize here that the slip velocities at the solid-liquid interface of the VP scheme are not expected to be equal to the slip velocities attained with the TW scheme, since the latter depend at least on the spring stiffness,[75] the mass of the wall atoms[76] and the solid-liquid LJ interaction strength.[41,84,85] In other words, the validation of the VP scheme does not require the achievement of the same slip velocity obtained with the TW scheme. Nonetheless, we have verified (not shown here) that the VP slip velocities, which are overall smaller than the TW scheme owing to the added VP-water LJ interactions, can be made similar to the TW results by varying d_{gv}, which has a significant impact on the slip properties at the interface, as will be explained.

Fig. 4 compares the equilibrium density profile when using the VP thermostat, against the TW scheme profile. Almost overlapping profiles demonstrate that structural properties of water near the interfaces and in the bulk are not significantly affected by the VP scheme, when compared with the classical TW approach. However, the first peak of the density profile for the VP system appears slightly shifted towards the wall and with higher amplitude, compared with the TW profile. This can be ascribed to the higher degree of hydrophilicity of the composed system graphene-VP plane, with respect to the graphene alone.

The density profiles show that the effective channel width is different from the distance between the two graphene layers' center of mass separation, $h = 2.57$nm. The effective channel width is estimated subtracting out the graphene interatomic radii, i.e., $h_{eff} = 2.57 - (\sigma_{CO} + \sigma_{CO})/2 \sim 2.25$ nm, since water is depleted at the interface. Note that to plot the velocity profiles of Fig. 2 and the temperature profiles of Fig. 3, the horizontal axis (channel) width considered is $h' \lesssim h_{eff}$, to avoid the statistical noise in the bins immediately adjacent the interfaces.

All the temperature profiles obtained in this work exhibit weak temperature gradients and, to a good approximation, they may be considered flat. Hence in the following, instead of plotting the full temperature profiles we only consider the value of the temperature at the center of the channel (which corresponds to the bin $N = 50$), and we plot this value as

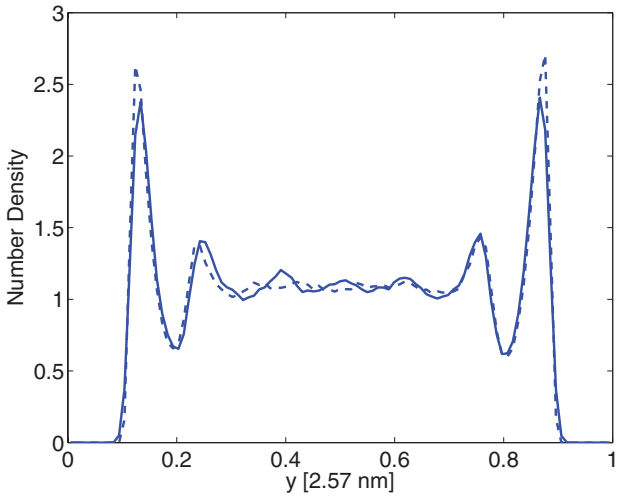

FIG. 4. Equilibrium density profile of water. VP scheme plotted with the dashed line, and TW scheme with the solid line.

a function of the varying parameter under investigation, to improve the readability of the data trends. Similarly, the velocity profiles all manifest a parabolic shape, typical of the Poiseuille flow profile, and our analysis will mostly require the knowledge of the velocity slip, i.e. the value of the velocity near the interface. Thus in what follows, we choose the bin $N = 20$ and plot the corresponding velocity value as a function of the parameter under investigation.

We investigate the effect of varying d_{gv}, and plot streaming velocity and temperature profiles in Figs. 5(a) and 5(b), respectively (square symbols). Again, reference parameters are $\sigma_{wVP} = 0.3166$ nm, $\epsilon_{wVP} = 0.6502$ kJ/mol, $k_{VP} = 0.431$ Nm^{-1}, and $N_{VP} = 36$ particles per virtual plane, with $F = 2.56 \times 10^{13}$ ms^{-2} and exploring the range -0.32 Å $\leq d_{gv} \leq 1.27$ Å. Gradually increasing d_{gv} from -0.32 Å to 1.27 Å monotonically decreases the velocity slip at the boundaries. For $d_{gv} = -0.32$ Å the equilibrium position of the thermostatting plane particles is behind graphene, reducing its momentum exchange with water. Thus, for that position, the temperature is the highest, $T \sim 380$ K, and the slip velocity attains its maximum $v_x \sim 500$ ms^{-1}. Shifting the VP plane inside the fluid, fixing $d_{gv} = 1.27$ Å, attaches corrugation to the rigid structure, increasing opportunities for water to exchange momentum with the thermostat, as seen with the lowest $T \sim 310$ K and $v_x \sim 200$ ms^{-1}. The decreasing trend of the temperature is not linear, flattening towards $T \approx 300$ K, the thermostat temperature.

We also plot in Figs. 5(a) and 5(b) results obtained when the VP oscillation is not constrained to only occur in the y-direction, but is allowed to in the x, y, z directions (VP-3D scheme). Data show similar trends, with the VP scheme yielding temperatures lower than the VP-3D scheme.

Fig. 5(c) depicts density profiles as a function of d_{gv} for the VP case. Note that the density profiles for the VP-3D case are not shown since they are similar to the VP case. When $d_{gv} = -0.32$ Å (red profile), the first peak acquires the highest amplitude. The prevailing influence of the rigid, hydrophobic wall structures the water molecules close to the interface. Shifting the VP plane inside the fluid adds roughness which induces disorder in the first adsorbed liquid layer, lowering the amplitude of the first peak. The bulk density appears unaffected overall.

In order to investigate the effect of changing the number of the VP particles we consider a rectangular, dense grid of $N_{VP} = 72$ particles per plane (within the VP scheme), plotting velocity results in Fig. 6, which also depicts results for the case $N_{VP} = 72$, but employing the VP-3D scheme. As a reference we set $\sigma_{wVP} = 0.3166$ nm, $\epsilon_{wVP} = 0.6502$ kJ/mol, $k_{VP} = 0.431$ Nm^{-1}, $d_{gv} = 0.63$ Å, and again the field is in the range $F = (1.28 - 6.42) \times 10^{13}$ ms^{-2}. Note that in the same picture, for comparison purposes, we show results for the VP scheme using $N_{VP} = 36$ (same as Fig. 2) and the VP-3D scheme with $N_{VP} = 36$. VP and VP-3D slip velocities are quite similar for $N_{VP} = 36$. Similarly, for $N_{VP} = 72$ the two implementations VP and VP-3D yield comparable results. Note that the $N_{VP} = 36$ slip velocities (for both VP and VP-3D) are larger than the (VP and VP-3D) $N_{VP} = 72$ slip velocities, coherently with the larger hydrophilicity of the $N_{VP} = 72$ plane.

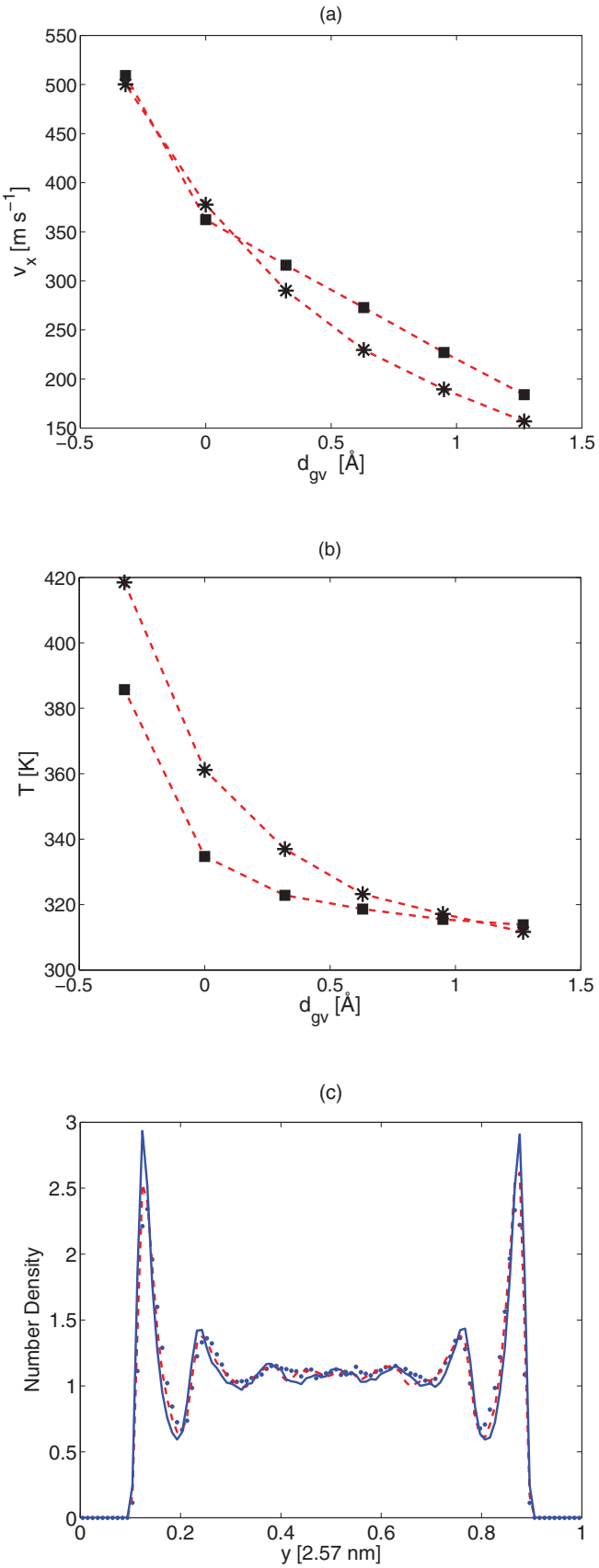

FIG. 5. (a) Slip velocity evaluated at the bin $N = 20$ (which is close to the interface). (b) Temperatures of water evaluated at the central bin ($N = 50$) of the temperature profile for -0.32 Å $\leq d_{gv} \leq 1.27$ Å. VP case depicted with squares, VP-3D with asterisks. (c) Density profile of water for VP. The case $d_{gv} = -0.32$ Å is depicted with the blue solid line, $d_{gv} = 0.63$ Å with the dashed red line and $d_{gv} = 1.27$ Å with the blue dotted line.

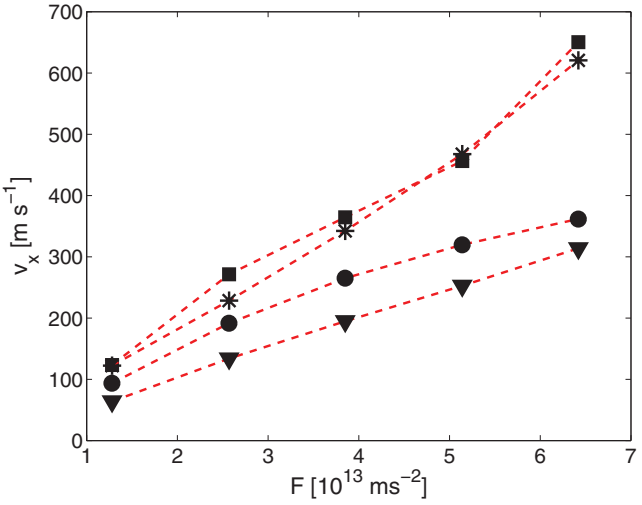

FIG. 6. Slip velocity evaluated at the bin $N = 20$ (which is close to the interface) of the streaming velocity profile of water for the fields $F = (1.28–6.42) \times 10^{13}$ ms^{-2}. Squares depict results obtained with the VP scheme ($N_{VP} = 36$), asterisks with VP-3D ($N_{VP} = 36$), circles with VP and $N_{VP} = 72$, triangles with VP-3D and $N_{VP} = 72$.

The temperature results relative to Fig. 6 are plotted in Fig. 7, with identical meaning of symbols and same reference parameters. Fig. 7 also plots the TW temperatures illustrated in Fig. 3(b). Using $N_{VP} = 72$ (within the VP scheme) has a striking effect on the fluid temperature, which is kept at $T \sim 310$ K, even at the highest field. The performance resembles, to some extent, the temperature control achievable by directly thermostatting the fluid. We emphasize the importance of this characteristic, since the VP scheme may not only substitute the direct application of the thermostat to the fluid, but concomitantly may provide an approximate *a priori* control of the temperature state point. Note that within the VP-3D scheme the case $N_{VP} = 72$ yields $T \sim 340$ K. If we compare the temperatures in Fig. 7, we find that as

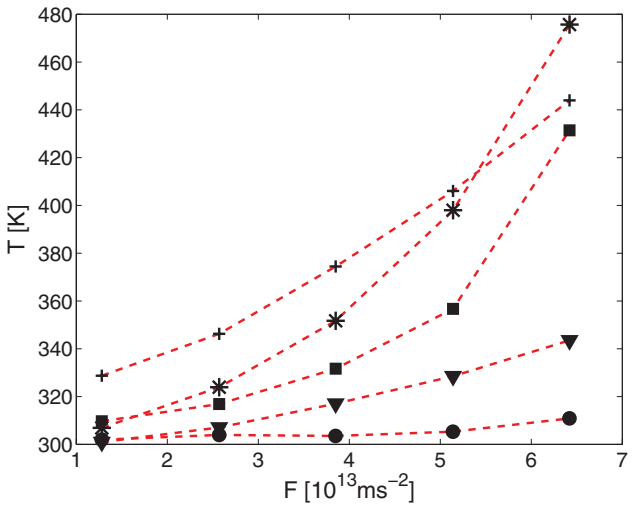

FIG. 7. Temperature of water evaluated at the central bin ($N = 50$) of the temperature profile for the field $F = (1.28–6.42) \times 10^{13}$ ms^{-2}. Squares depict results obtained with the VP scheme ($N_{VP} = 36$), asterisks with VP-3D ($N_{VP} = 36$), circles with VP and $N_{VP} = 72$, triangles with VP-3D and $N_{VP} = 72$, plus sign with the TW scheme.

field strength increases from $F = 1.28 \times 10^{13}$ ms^{-2} to $F = 5.14 \times 10^{13}$ ms^{-2} the TW scheme yields higher temperatures than the other cases. However, this depends on the particular set of VP parameters used for the comparison. For instance, observing $F = 2.56 \times 10^{13}$ ms^{-2}, Fig. 7 shows that the TW fluid temperature is $T \sim 345$ K, higher than the other VP temperatures $T \lesssim 320$ K. Even so, varying d_{gv} enables to attain almost the same temperature, as can be seen in Fig. 5(b), where at the same field and with $d_{gv} = 0$ one observes $T \sim 340$ K. We will provide in the following discussion other two specific sets of VP parameters such that at $F = 2.56 \times 10^{13}$ ms^{-2} the VP scheme is able to attain the TW temperature ~345 K, evidencing the flexibility of our strategy. At the highest $F = 6.42 \times 10^{13}$ ms^{-2} the VP and VP-3D schemes with $N_{VP} = 36$ attains similar or larger temperatures than the TW scheme, but doubling N_{VP} allows again $T_{VP} < T_{TW}$ for every field (and for both VP and VP-3D). Note that the VP-3D temperatures (for $N_{VP} = 36$ and $N_{VP} = 72$) are always higher than the corresponding VP temperatures. This is due to the VP constrained motion in the y-direction, which as explained, reduces the thermal speed of water at the interface. The TW and VP temperatures manifest a similar (in this case, nonlinear) dependence on the force, as can be seen in Fig. 7, except for $N_{VP} = 72$ in which the fluid temperature ranges in the small interval 300–330 K for every field.

Density profiles are depicted in Fig. 8 with $N_{VP} = 72$ (VP-3D and VP) and TW displaying almost overlapping profiles and $N_{VP} = 36$ (VP-3D and VP) having larger first peak amplitudes. The highest amplitude is obtained with (VP) $N_{VP} = 36$. The $N_{VP} = 36$ profiles are moderately shifted towards the interface, due to the smaller number of VP repulsive LJ sites. The TW profile has a marginally larger width with respect to the others, of the order of the dimension of one bin, corroborating the fact that the induced water structuring close to the solid is not significantly altered by the VP scheme, compared with the TW scheme. Finally, note that the liquid bulk densities appear similar for all the schemes. In the following, we consider only the VP density profiles, and not the VP-3D ones.

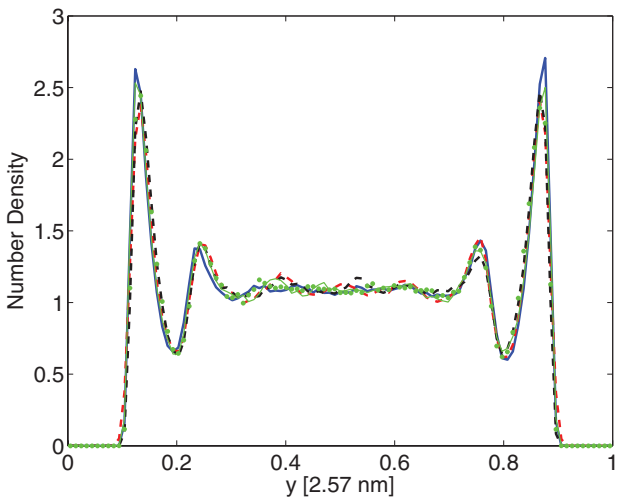

FIG. 8. Density profile for ($N_{VP} = 36$) VP scheme (blue solid line), TW (red dashed line), ($N_{VP} = 72$) VP (black dashed line), ($N_{VP} = 36$) VP-3D (green solid line), ($N_{VP} = 72$) VP-3D (green dotted line).

In Fig. 9(a), we investigate the effect of changing ϵ_{wVP}. Fixing $F = 2.56 \times 10^{13}$ ms^{-2}, and using the (previous) reference values $\sigma_{wVP} = 0.3166$ nm, $k_{VP} = 0.431$ Nm^{-1}, and $d_{gv} = 0.63$ Å, we explore the range $\epsilon_{wVP} = (0.52–0.78)$ kJ/mol. A gradual reduction of the velocity slip is detectable, as ϵ_{wVP} increases. This is expected since the stronger LJ interactions more intensely pack water at the interfaces, in agreement with literature results.[41,84,85] Note that for every ϵ_{wVP} we found $v_{(VP-3D)} < v_{VP}$, since the VP-3D scheme adds more roughness with respect to the VP scheme, reducing the slip velocity at the interface. We report in Fig. 9(b) the corresponding temperatures. As ϵ_{wVP} increases the temperature decreases, since stronger interactions enhance the energy transport at the interface. Density profiles are reported in Fig. 9(c) showing that changing ϵ_{wVP} does not lead to significant differences between profiles.

In Fig. 10(a) we investigate the effect σ_{wVP} has on the slip velocity and temperature. Again, $F = 2.56 \times 10^{13}$ ms^{-2}, and reference $\epsilon_{wVP} = 0.6502$ kJ/mol, $k_{VP} = 0.431$ Nm^{-1}, and $d_{gv} = 0.63$ Å (as before), but varying $\sigma_{wVP} = (0.253 - 0.443)$ nm. For $\sigma_{wVP} \lesssim \sigma_{SPC/E}$, larger values of σ_{wVP} yield VP planes exposing larger surface area to water, enhancing interactions and momentum exchange, thereby reducing the slip velocity. On the other hand, when the VP diameters increase in the range $\sigma_{wVP} > \sigma_{SPC/E}$, the Lennard-Jones landscape potential experienced by water will be more regular, resulting in a smoother interface, hence increasing the slip velocity. The VP-3D scheme results depicted in the same picture shows roughly the same trend, but shifted towards larger σ_{wVP}. The disorder induced in the fluid by the added degree of freedom of the VP motion in the x, z directions add roughness to the water-wall interactions, reducing the slip velocity. For both the VP and VP-3D methods, see Fig. 10(b), increasing σ_{VP} corresponds to an expansion of the VP on the border of the fluid control volume, increasing the thermostatting efficiency, and lowering the fluid temperature. Note that in Fig. 10(b) $\sigma_{wVP} = 0.253$ nm provides $T = 343$ K, almost equal to the TW temperature $T \sim 345$ K attained at the same $F = 2.56 \times 10^{13}$ ms^{-2}, see Fig. 7.

Fig. 10(c) shows the density profiles. For the smallest value of $\sigma_{wVP} = 0.253$ nm the first peak next to the graphene layer is the highest, and most shifted towards the wall. As σ_{wVP} increases, the Lennard-Jones VP-water repulsion adds its contribution to the already existent graphene-water repulsion, shifting the peak towards the center. Again, the effect is small due to the smallness of the spring stiffness.

Finally, Fig. 11 reports the effect of changing the VP spring constant. As before $F = 2.56 \times 10^{13}$ ms^{-2}, with $\epsilon_{wVP} = 0.6502$ kJ/mol, $d_{gv} = 0.63$ Å, $\sigma_{wVP} = 0.3166$ nm, and $k = (0.11–3.23)$ Nm^{-1}. Note that $k = 3.23$ Nm^{-1} has been used in our previous work.[60] The velocities are plotted in Fig. 11(a), showing two regimes for the slip velocity as a function of the spring stiffness. In the range $k = (0.1–1.5)$ Nm^{-1}, decreasing k increases the oscillation amplitudes of the VP, enhancing momentum transfer between VP and water molecules. The composite system graphene-VP plane exposes a rougher surface to water, as k decreases in the specified range, reducing the slip velocity at the interfaces. At the smallest k values, the momentum transfer between

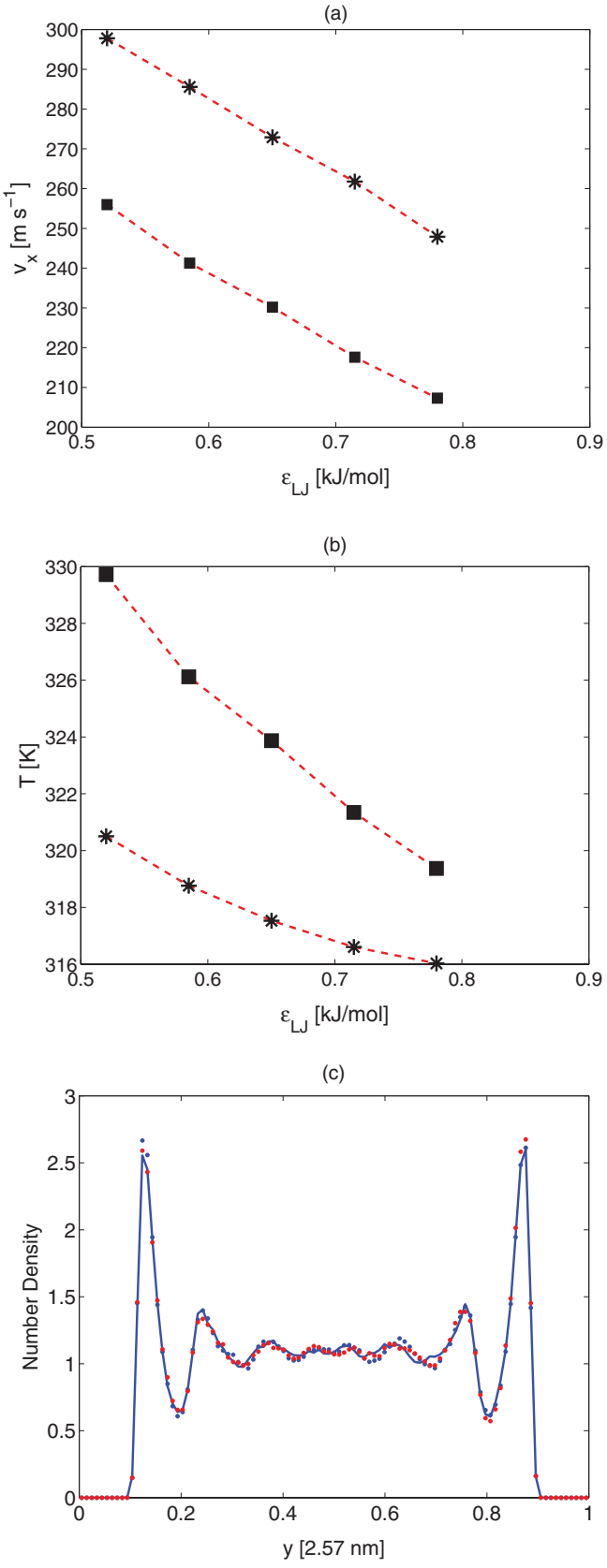

FIG. 9. (a) Slip velocity evaluated at the bin $N = 20$ (which is close to the interface) of the streaming velocity profile and (b) temperature of water evaluated at the central bin ($N = 50$) of the temperature profile for $\epsilon_{wVP} = (0.52–0.78)$ kJ/mol. Data points plotted with asterisks are obtained using VP, squares with VP-3D. (c) Density profiles of water. The case $\epsilon_{wVP} = 0.52$ kJ/mol is depicted with the blue solid line, the case $\epsilon_{wVP} = \epsilon_{SPC/E}$ with the blue dotted line and $\epsilon_{wVP} = 0.78$ kJ/mol with the red dotted line.

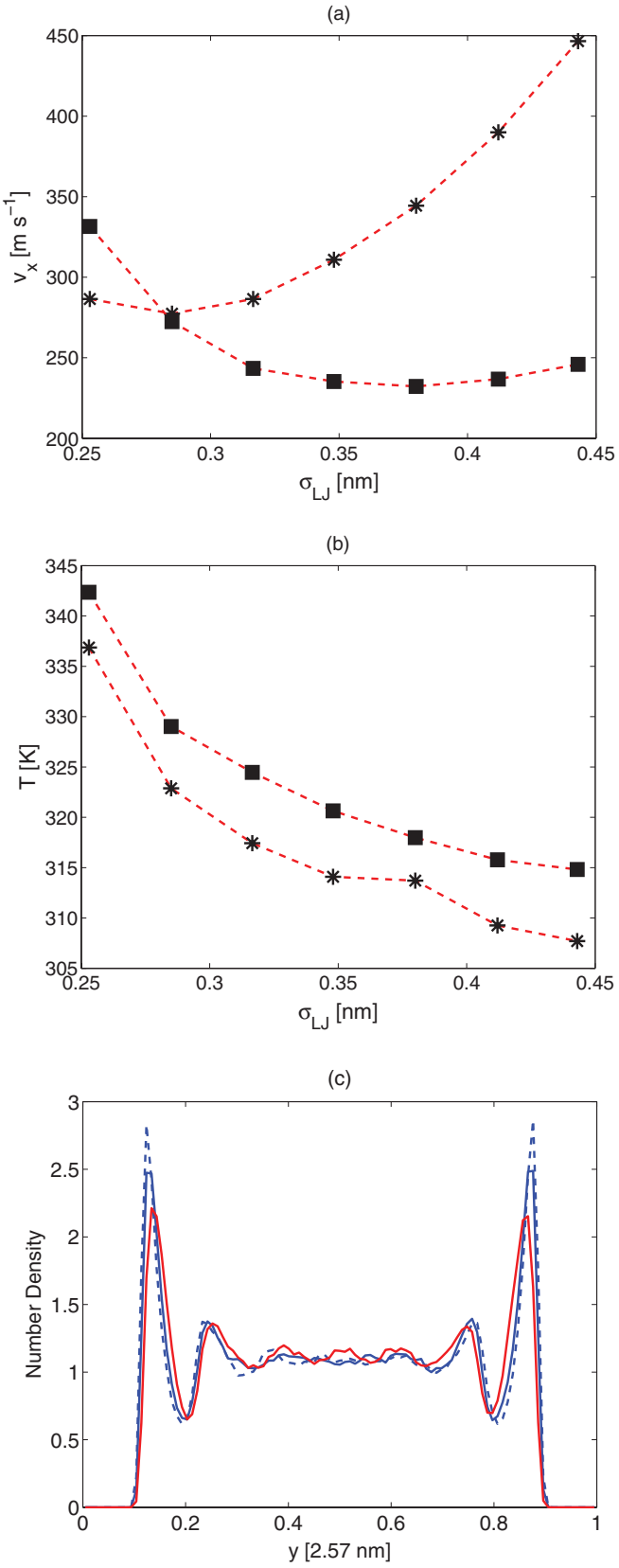

FIG. 10. (a) Slip velocity evaluated at the bin $N = 20$ (which is close to the interface) of the streaming velocity profile and (b) temperature of water evaluated at the central bin ($N = 50$) of the temperature profile for σ_{wVP} = (0.253–0.443) nm. Data points plotted with asterisks are obtained using VP, squares with VP-3D. (c) Density profiles of water. The case σ_{wVP} = 0.253 nm is depicted with blue dashed lines, $\sigma_{wVP} = 0.348$ nm with blue solid lines, and $\sigma_{wVP} = 0.443$ nm with red solid lines.

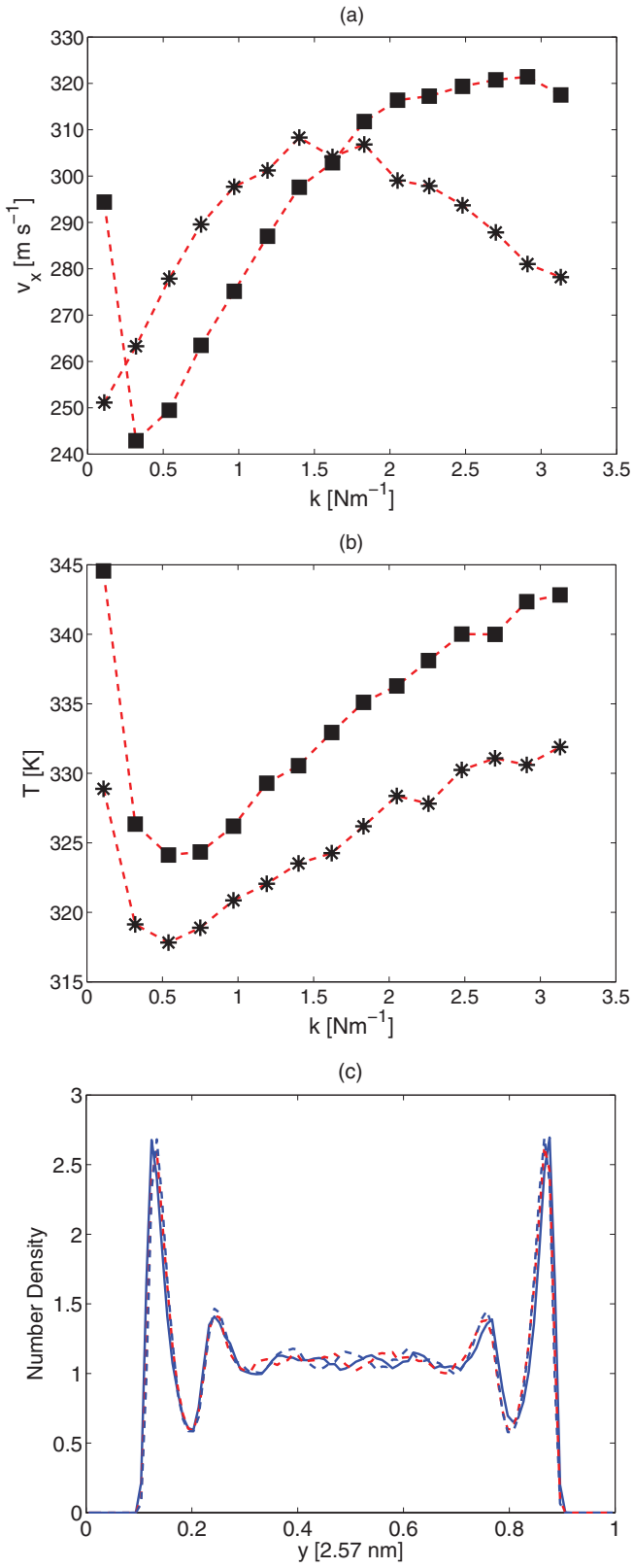

FIG. 11. (a) Slip velocity evaluated at the bin $N = 20$ (which is close to the interface) of the streaming velocity profile and (b) temperature of water evaluated at the central bin ($N = 50$) of the temperature profile of water for $k = 0.11 - 3.23$ Nm^{-1}. Data points represented with asterisks are obtained using VP, squares with VP-3D. (c) Density profiles of water. The case $k = 0.11$ Nm^{-1} is depicted with the blue solid line, the intermediate value $k = 1.83$ Nm^{-1} with the red dashed line and $k = 3.23$ Nm^{-1} with the dashed blue line.

water molecules and virtual particles is reduced because the average position of the virtual particles is shifted behind the rigid wall (the virtual particles center of mass is not conserved), making the (hydrophobic) interactions between the carbon atoms and water molecules dominant. Hence, for the VP-3D scheme the velocity slip at the interface is enhanced. Arguably, for the VP scheme, the same effect should be reproduced for even smaller k values (not employed in this work). However, when the spring stiffness takes on larger values (in the range $k = (1.5–3)$ Nm^{-1}) its influence on the VP oscillation amplitudes[75,76] is reduced, which in turn will depend mainly on the temperature of the VP. At that point, larger k will only increase the frequency of the oscillations, leading to improved momentum transfer which reduces the slip velocity. Note that, in the framework of thermal walls, a detailed analysis of the effect of the wall stiffness on the slip at the boundary has been given by Asproulis and Drikakis,[75] who demonstrated that the slip length dependence on the wall stiffness can be represented by a fifth-order polynomial that qualitatively resembles the trend in Fig. 11(a).

The temperatures for the full range $k = (0.1–3)$ Nm^{-1} are reported in Fig. 11(b), where a minimum is observed at $k \sim 0.5$ Nm^{-1} and the temperatures gradually increase. As the spring constant increases, the frequency of the oscillations increase, leading to an improved momentum transfer between water molecules and the virtual particles. However, this does not correspond to an improved energy absorption, since the virtual particles are subjected to a greater acceleration (as k increases), pumping more energy into the fluid system. For $k \lesssim 0.5$ Nm^{-1} the virtual particles position is on average shifted behind the graphene surface by the collisions with water molecules. In this regime, the thermostat becomes less efficient because water molecules predominantly interact with the rigid graphene surface, hence, the momentum transfer between water molecules and virtual particles is reduced. Note that as a reference parameter for the spring constant we have always used $k_{VP} = 0.431$ Nm^{-1}, which yields approximately the best thermostatting performance, as can be seen in Fig. 11(b) where the fluid temperature minimum is achieved around $k_{VP} = 0.5$ Nm^{-1}. Density profiles for $k = (0.11–3.23)$ Nm^{-1} are shown in Fig. 11(c), showing that the fluid layering next to the interface is not significantly affected for the k_{VP} range examined here. Note that the VP-3D results depicted in Fig. 11(a) are shifted to the right with respect to the VP ones, maintaining qualitatively the same characteristic global shape, and the VP temperatures are systematically smaller than the VP-3D case, as already observed. Again, also varying the VP spring constant k allows to achieve the same TW thermostatting performance, noting that for $k_{VP} = 0.11$ Nm^{-1} it is observed $T = 345$ K (Fig. 11(b)), coincident with the TW temperature $T \sim 345$ K attained at the same $F = 2.56 \times 10^{13}$ ms^{-2}, see Fig. 7.

We conclude the discussion on the effects of the VP parameters suggesting that a good initial choice of the VP parameters may be $\sigma_{wVP} = 0.3166$ nm, $\epsilon_{wVP} = 0.6502$ kJ/mol (same as the liquid LJ parameters), $k_{VP} = 0.431$ Nm^{-1}, $d_{gv} = 0.63$ Å (VP plane slightly shifted inside the fluid), and $N_{VP} = 36$ particles per virtual plane, in conjunction with the VP scheme (and not the VP-3D scheme). This initial description yields the temperature minimum ($T \simeq 318$ K) in Fig. 11(b), attained with the VP scheme (the VP-3D scheme yields $T \simeq 325$ K, hence it is less efficient in absorbing heat) and, as will be detailed in Sec. IV, provides reasonable values for the thermal boundary resistance. Note that the fluid output temperature may vary for different sizes, materials, and geometries of the confining systems, given the external force strengths employed in this work. Moreover, we point out that if the focus is on an accurate reproduction of the thermal boundary resistance or a reproduction of the slip properties of a particular solid/liquid interface, a more careful tuning of the VP parameters may be required. Nonetheless, the flexibility of this scheme should allow for a good thermostatting performance simultaneously allowing for a good reproduction of other solid/liquid interface properties, particularly if the external field is not strong.

Fig. 12 illustrates the time history of the total center of mass kinetic energy for the case examined at the beginning of this section, see Fig. 2. For the field range $F = (1.28–6.42) \times 10^{13}$ ms^{-2} we report the kinetic energy comparing the TW and VP methods ($N_{VP} = 36$). It can be seen that the amplitude of the oscillations around the respective average kinetic energy is similar for both, and the initial kinetic energy transient lasts approximately the same time interval.

IV. THERMAL RESISTANCE

In Sec. III we showed that the VP scheme reproduces the temperature discontinuity at the solid-liquid interface,[82,83] since a heat flux crosses a boundary between two different materials. At $T_{VP} = 298$ K, the fluid attains different temperatures, depending on the external field and the VP parameters. To further validate the VP method, we compute the Kapitza resistance[66,67] at the solid-liquid interface, with the solid part considered to be the combined system of rigid wall-VP. Note that our aim is not to evaluate exactly the Kapitza resistance at the water-graphene interface, but to show that heat fluxes and thermal boundary resistances involved in our scheme

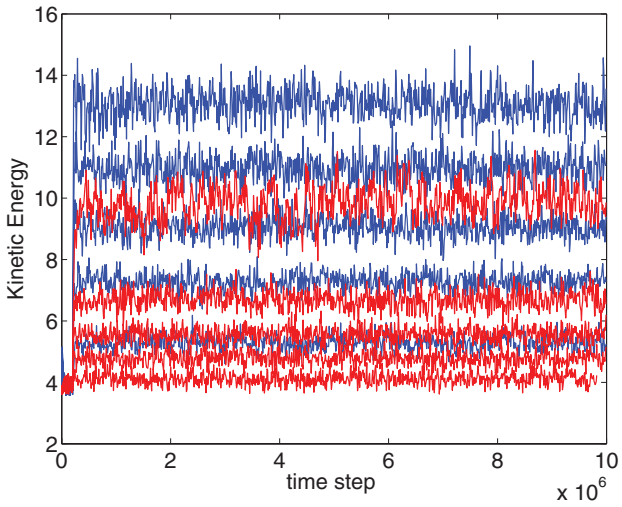

FIG. 12. Kinetic energy time history of water for $F = (1.28–6.42) \times 10^{13}$ ms^{-2}. The TW case is colored in blue and VP in red ($N_{VP} = 36$).

are within the range of known experimental and MD results. An accurate characterization of the Kapitza resistance at the solid-liquid interface would require a different protocol.[86,87] Given the heat flux J_q, that is, the amount of heat passing through the surface per unit time, and the temperature drop $\Delta T = T_f - T_w$ across the interface, the boundary thermal resistance is quantified by

$$R = \frac{\Delta T}{J_q}. \tag{15}$$

Hence, an estimate of the heat flux and temperature profile is necessary to evaluate R. To compute the heat flux vector normal to the interface, we use the direct integration of the energy continuity equation, i.e., the IEC method.[88–90] The hydrodynamical balance equation for the specific internal energy is

$$\rho \frac{dU(\mathbf{r},t)}{dt} = -\nabla \cdot \mathbf{J}_q(\mathbf{r},t) - \mathbf{P}^T(\mathbf{r},t) : \nabla \mathbf{v}(\mathbf{r},t), \tag{16}$$

where the quantity of interest is the heat flux vector $\mathbf{J}_q(\mathbf{r},t)$. The quantities ρ, $U(\mathbf{r},t)$, $\mathbf{P}^T(\mathbf{r},t)$, and $\mathbf{v}(\mathbf{r},t)$ represent the mass density, the internal energy per unit mass of the fluid, the transpose of the pressure tensor, and the streaming velocity of the fluid, respectively. In the steady-state, i.e., $dU(\mathbf{r},t)/dt = 0$, our Poiseuille flow geometry, with constant external gravity-like field applied in the x-direction and fluid confined between two planar surfaces parallel to the $x-z$ plane, leads to

$$\frac{dJ_{qy}(y)}{dy} = -P_{xy}(y)\dot{\gamma}(y) \tag{17}$$

with the strain rate given as

$$\dot{\gamma}(y) = \frac{\partial v_x(y)}{\partial y} \tag{18}$$

and the shear stress $-P_{xy}(y)$. Integrating along the y-direction (the so-called IEC method[88,89]) gives the heat flux,

$$J_{qy}(y) = -\int_0^y P_{xy}(y')\dot{\gamma}(y')dy'. \tag{19}$$

The stress profile $P_{xy}(y)$ can be evaluated with the IMC technique,[90] i.e., integrating the momentum continuity equation

$$P_{xy}(y) = F_e \int_0^y n(y')dy', \tag{20}$$

where F_e is the external force applied to hydrogen and oxygen atoms and $n(y')$ is the number density (NEMD) profile across the channel. A different route could have been followed to evaluate the heat flux,[91] averaging Eq. (3) in the steady state, and computing the rate of heat flux $J_q = \frac{\langle \Delta E(t) \rangle}{\Delta t A}$ where Δt is the time step, and A is the $x-z$ direction wall surface area. However, in our specific case, we have found that the quantity $\langle \Delta E \rangle$ exhibits poor statistical convergence.

The IMC and IEC methods have been applied to the VP case with $F = 2.57 \times 10^{13}$ ms^{-2}, $\sigma_{wVP} = 0.3166$ nm, $\epsilon_{wVP} = 0.6502$ kJ/mol, $k_{VP} = 0.431$ Nm^{-1}, $d_{gv} = 0.63$ Å, and $N_{VP} = 36$, shown in Fig. 2. The measurements have been taken in the steady state. The strain rate $\dot{\gamma}(y)$, shear stress $P_{xy}(y)$ and heat flux $J_{qy}(y)$ are plotted in Figs. 13(a)–13(c),

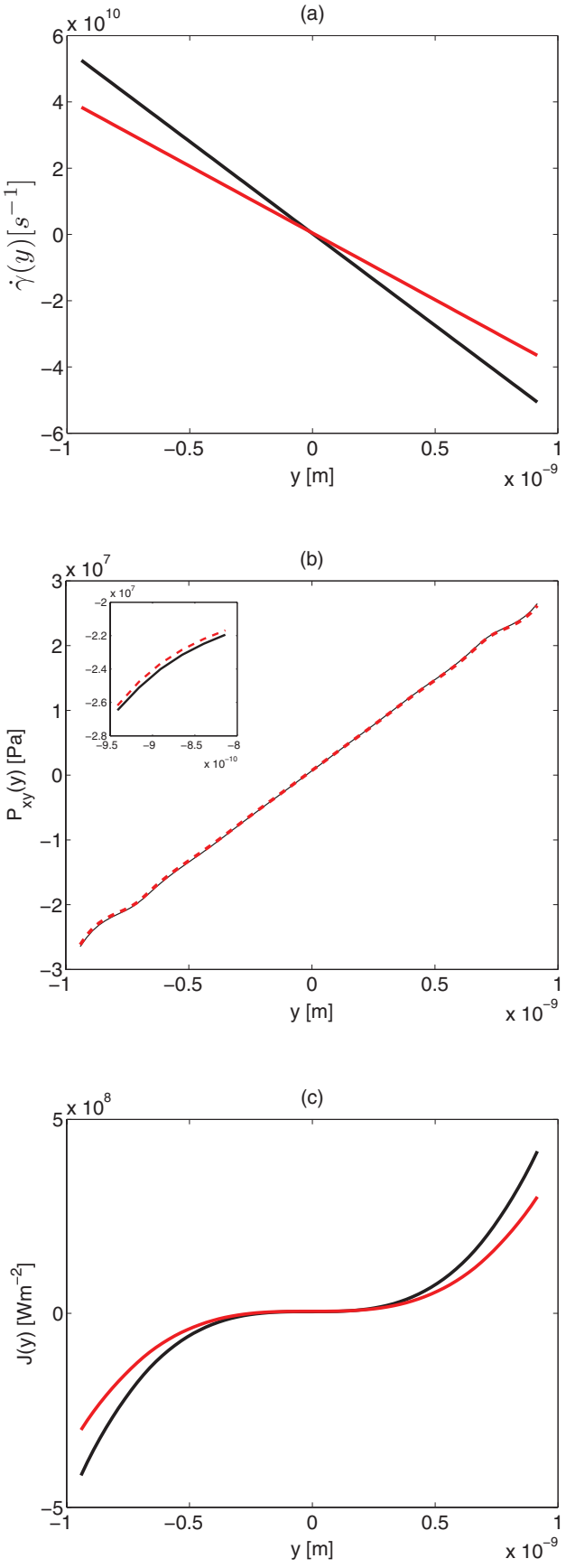

FIG. 13. (a) Strain rate of water across the channel, symmetrized with respect to the center of the channel, (b) shear stress with the detail near the boundary plotted in the inset, (c) heat flux for $F = 2.57 \times 10^{13}$ ms^{-2}. The VP ($N_{VP} = 36$) case is colored in red (dashed red line in part (b)) and TW in black solid line.

respectively. In the same plots, we compare results with the TW scheme for the same external field. As expected,[89,90] the shear stress is linear across the channel except close to the walls, and the heat flux has a cubic shape. It is important to note that the shear stress for the VP case and the TW case are approximately equal (apart from details at the boundary shown in the inset of Fig. 13(b)), demonstrating that the VP scheme does not exert unrealistic forces on the fluid. However, noting that $P_{xy} = -\eta\dot{\gamma}$ where η is the shear viscosity, it seems a contradictory finding that P_{xy} is almost equal for the TW and VP case (Fig. 13(b)), whereas the strain rate is different (Fig. 13(a)). This can be explained by the dependence on the temperature of the shear viscosity, noting that the temperature of the fluid is $T \sim 318$ K for the VP case, and $T \sim 350$ K for TW, as can be seen in Fig. 7. The consistency of the result can be verified considering that the viscosity for TW takes a lower value than VP (owing to the TW higher temperature) and the strain rate is larger than VP, see Fig. 13(a). The temperature discontinuity at the interface is $\Delta T = 17$ K (from $T_{wall} = 298$ K and T_{fluid} from Fig. 3(a)). Equation (15) gives $R = 4.2 \times 10^{-8}$ m^{2}KW^{-1}, which is approximately in the range of experimental[92,93] and MD[86,94] values for the solid-liquid Kapitza resistances $R \sim (2 \times 10^{-8} - 2 \times 10^{-9})$ m^{2}KW^{-1}.

To qualitatively check the consistency of the method, we further study the effect of varying d_{gv} on R, in the range -0.32 Å $\leq d_{gv} \leq 1.27$ Å, see Fig. 5. Results are ordered in Table I. We observe the decrease of R when the VP plane is shifted inside the channel, an expected result considering that the thermostat absorbs heat more efficiently if it is positioned in contact with water.

If instead of the LJ potential we use the Weeks-Chandler-Andersen (WCA) potential[95] for the water-VP interactions (but keep the attractive part of the rigid graphene), we find (not shown here) that for $F \leq 5.14 \times 10^{13}$ ms^{-2}, even with this completely repulsive potential the fluid system does not heat up excessively and temperature discontinuities at the interface are still detectable. They are higher but of the same order of the LJ case, plotted in Fig. 3(a). This agrees qualitatively with the theoretical discussion of Xue *et al.*[87] which (in the context of LJ fluids and for nonwetting solids) stated that even when there is no liquid-solid attraction the elastic collisions contribute to the energy transfer between liquid and solid preserving the finiteness of the Kapitza resistance.

TABLE I. Temperature jump, strain rate, shear stress, heat flux, and thermal boundary resistances as a function of d_{gv}. The point y_0 at which the properties are evaluated is close to the interface. Reference parameters and external field are indicated in the text.

d_{gv} (10^{-9} m)	ΔT (K)	$\gamma(y_0)$ (10^{11} s^{-1})	$P_{xy}(y_0)$ (10^7 Pa)	$J_{qy}(y_0)$ (10^9 Wm^{-2})	R (10^{-8} m^{2}KW^{-1})
0.127	14	0.41	3.04	0.4	3.5
0.095	15	0.4	3.04	0.39	3.9
0.063	19	0.42	3.04	0.41	4.6
0.032	23	0.45	3.04	0.43	5.3
0	35	0.53	3.04	0.51	6.8
−0.032	86	0.85	3.03	0.82	10.4

V. CONCLUSION

Contrary to existing thermostatting strategies for confined fluids, we have developed a simple scheme which enables the use of a frozen solid surface, without directly coupling the fluid with a thermostat. The scheme works by distributing a rectangular grid of virtual particles (oscillating on a plane close to the rigid wall) which function as heat absorbers for the unthermostatted water molecules. The spring constant of the virtual particles is lower than values required to conserve the solid state phase of the wall, and proper spring stiffnesses can be chosen without being constrained by the Lindemann criterion for melting. In consequence, the VP particle amplitude and frequency oscillations are higher and lower, respectively, than typical thermal wall implementations.

It has been demonstrated that our scheme does not significantly alter the mechanical properties of water confined between graphene surfaces, providing uniform temperature profiles and parabolic velocity profiles, as expected under Poiseuille flow. Moreover, the flexibility conferred by the several parameters at our disposal can be exploited to achieve fluid temperatures comparable to those attained with thermal walls, simultaneously preserving important characteristics of the slip velocity behaviour at the solid-liquid interface. Additionally, we reported three sets of VP parameters such that the temperature attained is almost equal to the temperature obtained with the thermal wall approach.

By computing the solid-liquid Kapitza resistance, we showed that the VP strategy realistically removes heat from the fluid, resembling an actual experiment. This may be an advantage if rigid walls are to be used, since directly thermostatting the fluid is an unphysical procedure. Note that in our scheme, as in NEMD runs with thermal walls, the fluid temperature is an outcome of the simulations, and may not be known a priori. However, we addressed this point by showing that it is possible to achieve better control of the final temperature by increasing the number of the VP particles. We further emphasize that fluid molecule permeation through the wall is suppressed by the rigidity of the real wall and that the low oscillation frequencies of the virtual particles allow simulations with larger MD time step.

The VP method requires preliminary runs for the optimal choices of the several parameters used. However, in this work we have provided some reliable estimates of these parameters, validated for liquid water confined between two (solid) graphene surfaces. Moreover, we elucidated the necessary conditions on which the VP parameters must rely.

Our scheme has been applied to two planar, neutral surfaces, however the method can be adapted to different geometries, like cylindrical carbon nanotubes and charged surfaces such as silica walls. An advantage of the VP scheme over standard techniques emerges when complex charged surfaces, as the (111) Miller plane of β-cristobalite, confine polar fluids like water. If the charged surface is thermalized then it may be difficult to find spring constant values such that structural stability is preserved simultaneously maintaining a good thermostatting performance. In our scheme, the charged walls can be kept rigid without directly applying a thermostat to the fluid.

Finally, we underline that the computational cost of our strategy is substantially reduced with respect to the thermal wall approach, since walls are rigid. Moreover, the method is $O(N_{VP})$, and N_{VP} is not related to the number of atoms composing the real wall, which can be made considerably larger since they do not need to be thermalized.

ACKNOWLEDGMENTS

Computational resources were provided by the Swinburne Supercomputer Centre, the Victorian Partnership for Advanced Computing HPC Facility and Support Services and an award under the Merit Allocation Scheme on the NCI National Facility at the Australian National University. J.S.H. acknowledges Lundbeckfonden for supporting this work as a part of Grant No. R49-A5634.

[1] B. J. Kirby, *Micro- and Nanoscale Fluid Mechanics: Transport in Microfluidic Devices* (Cambridge University Press, Cambridge, 2010).
[2] W. Xiong, J. Z. Liu, M. Ma, Z. Xu, J. Sheridan, and Q. Zheng, Phys. Rev. E **84**, 056329 (2011).
[3] B. Xu, B. Wang, T. Park, Y. Qiao, Q. Zhou, and X. Chen, J. Chem. Phys. **136**, 184701 (2012).
[4] J. A. Thomas, A. J. H. McGaughey, and O. Kuter-Arnebeck, Int. J. Therm Sci. **49**, 281 (2010).
[5] K. P. Travis, P. J. Daivis, and D. J. Evans, J. Chem. Phys. **103**, 1109 (1995).
[6] J. L. McWhirter and G. N. Patey, J. Chem. Phys. **117**, 2747 (2002).
[7] N. V. Priezjev and S. M. Troian, Phys. Rev. Lett. **92**, 018302 (2004).
[8] D. M. Huang, C. Cottin-Bizonne, C. Ybert, and L. Bocquet, Langmuir **24**, 1442 (2008).
[9] I. C. Bourg and C. I. Steefel, J. Phys. Chem. C **116**, 11556 (2012).
[10] H. J. C. Berendsen, J. P. M. Postma, W. F. van Gunsteren, A. DiNola, and J. R. Haak, J. Chem. Phys. **81**, 3684 (1984).
[11] G. S. Grest and K. Kremer, Phys. Rev. A **33**, 3628 (1986).
[12] D. J. Evans and G. P. Morriss, *Statistical Mechanics of Nonequilibrium Liquids* (Cambridge University Press, Cambridge, 2008).
[13] H. Andersen, J. Chem. Phys. **72**, 2384 (1980).
[14] L. Lue, O. G. Jepps, J. Delhommelle, and D. J. Evans, Mol. Phys. **100**, 2387 (2002).
[15] K. P. Travis and C. Braga, J. Chem. Phys. **128**, 014111 (2008).
[16] S. Nosé, J. Chem. Phys. **81**, 511 (1984).
[17] S. Nosé, Mol. Phys. **52**, 255 (1984).
[18] W. G. Hoover, Phys. Rev. A **31**, 1695 (1985).
[19] D. Frenkel and B. Smit, *Understanding Molecular Simulation. From Algorithms to Applications*, 2nd ed. (Academic Press, USA, 2001).
[20] M. P. Allen and T. J. Tildesley, *Computer Simulation of Liquids* (Clarendon Press, Oxford, 1987).
[21] D. Rapaport, *The Art of Molecular Dynamics Simulation*, 2nd ed. (Cambridge University Press, New York, 2004).
[22] M. E. Tuckerman, *Statistical Mechanics: Theory and Molecular Simulation* (Oxford University Press, New York, 2010).
[23] R. J. Sadus, *Molecular Simulation of fluids: Theory, Algorithms and Object-Orientation* (Elsevier, Amsterdam, 1999).
[24] S. K. Kannam, B. D. Todd, J. S. Hansen, and P. J. Daivis, J. Chem. Phys. **138**, 094701 (2013).
[25] F. Schedin, A. K. Geim, S. V. Morozov, E. W. Hill, P. Blake, M. I. Katsnelson, and K. S. Novoselov, Nature Mater. **6**, 652 (2007).
[26] Y. M. Lin, C. Dimitrakopoulos, K. A. Jenkins, D. B. Farmer, H. Y. Chiu, A. Grill, and P. Avouris, Science **327**, 662 (2010).
[27] D. Cohen-Tanugi and J. C. Grossman, Nano Lett. **12**, 3602 (2012).
[28] N. V. Priezjev, J. Chem. Phys. **136**, 224702 (2012).
[29] P. A. Thompson and M. O. Robbins, Phys. Rev. A **41**, 6830 (1990).
[30] D. J. Evans and G. P. Morriss, Phys. Rev. Lett. **56**, 2172 (1986).
[31] K. P. Travis, P. J. Daivis, and D. J. Evans, J. Chem. Phys. **103**, 10638 (1995).
[32] U. Heinbuch and J. Fischer, Phys. Rev. A **40**, 1144 (1989).
[33] S. Y. Liem, D. Brown, and J. H. R. Clarke, Phys. Rev. A **45**, 3706 (1992).
[34] P. Padilla and S. Toxvaerd, J. Chem. Phys. **104**, 5956 (1996).
[35] W. G. Hoover, C. G. Hoover, and J. Petravic, Phys. Rev. E **78**, 046701 (2008).
[36] P. J. Daivis, B. A. Dalton, and T. Morishita, Phys. Rev. E **86**, 056707 (2012).
[37] S. Bernardi, B. D. Todd, and D. J. Searles, J. Chem. Phys. **132**, 244706 (2010).
[38] X. Yong and L. T. Zhang, J. Chem. Phys. **138**, 084503 (2013).
[39] K. P. Travis, P. J. Daivis, and D. J. Evans, J. Chem. Phys. **105**, 3893 (1996).
[40] J. P. Hansen and I. R. McDonald, *Theory of Simple Liquids*, 3rd ed. (Academic Press, London, 2006).
[41] A. Jabbarzadeh, J. D. Atkinson, and R. I. Tanner, J. Chem. Phys. **110**, 2612 (1999).
[42] D. W. Brenner, Phys. Rev. B **42**, 9458 (1990).
[43] B. H. Kim, A. Beskok, and T. Cagin, Microfluid. Nanofluid. **5**, 551 (2008).
[44] B. H. Kim, A. Beskok, and T. Cagin, J. Chem. Phys. **129**, 174701 (2008).
[45] J. C. Tully, J. Chem. Phys. **73**, 1975 (1980).
[46] J. Blömer and A. E. Beylich, Proc. Int. Symp. Rarefield Gas Dyn. 392–397 (1996).
[47] T. Kimura and S. Maruyama, Microscale Thermophys. Eng. **6**, 3 (2002).
[48] H. Berro, N. Fillot, P. Vergne, T. Tokumasu, T. Ohara, and G. Kikugawa, J. Chem. Phys. **135**, 134708 (2011).
[49] T. Ohara and D. Torii, J. Chem. Phys. **122**, 214717 (2005).
[50] S. C. Maroo and J. N. Chung, J. Nanopart. Res. **12**, 1913 (2010).
[51] S. De Luca, B. D. Todd, J. S. Hansen, and P. J. Daivis, "A molecular dynamics study of nanoconfined water flow driven by rotating electric fields under realistic experimental conditions," Langmuir (submitted).
[52] M. Gambhir, M. T. Dove, and V. Heine, Phys. Chem. Miner. **26**, 484 (1999).
[53] W. W. Schmahl, I. P. Swainson, M. T. Dove, and A. Z. Graeme-Barber, Kristallogr. **201**, 125 (1992).
[54] I. P. Swainson and M. T. Dove, J. Phys.: Condens. Matter. **7**, 1771 (1995).
[55] F. Liu, S. H. Garofalini, R. D. King-Smith, and D. Vanderbilt, Phys. Rev. Lett. **70**, 2750 (1993).
[56] L. Huang and J. Kieffer, J. Chem. Phys. **118**, 1487 (2003).
[57] L. T. Zhuravlev, Colloids Surf., A **173**, 1–38 (2000).
[58] H. J. C. Berendsen, J. R. Grigera, and T. P. Straatsma, J. Phys. Chem. **91**, 6269 (1987).
[59] M. A. Gonzalez and J. L. F. Abascal, J. Chem. Phys. **132**, 096101 (2010).
[60] S. De Luca, B. D. Todd, J. S. Hansen, and P. J. Daivis, J. Chem. Phys. **138**, 154712 (2013).
[61] T. R. Zeitler, J. A. Greathouse, and R. T. Cygan, Phys. Chem. Chem. Phys. **14**, 1728 (2012).
[62] J. Yang, S. Meng, L. Xu, and E. G. Wang, Phys. Rev. B **71**, 035413 (2005).
[63] J. Puibasset and R. J.-M. Pellenq, J. Chem. Phys. **119**, 9226 (2003).
[64] S. R.-V. Castrillón, N. Giovambattista, I. A. Aksay, and P. G. Debenedetti, J. Phys. Chem. B **113**, 1438 (2009).
[65] D. Argyris, D. R. Cole, and A. Striolo, J. Phys. Chem. C **113**, 19591 (2009).
[66] P. L. Kapitza, J. Phys (USSR) **4**, 181 (1941).
[67] J.-L. Barrat and F. Chiaruttini, Mol. Phys. **101**, 1605 (2003).
[68] G. Ciccotti, M. Ferrario, and J. P. Ryckaert, Mol. Phys. **47**, 1253 (1982).
[69] Y. S. Badyal, M.-L. Saboungi, D. L. Price, S. D. Shastri, D. R. Haeffner, and A. K. Soper, J. Chem. Phys. **112**, 9206 (2000).
[70] K. S. Novoselov, A. K. Geim, S. V. Morozov, D. Jiang, Y. Zhang, S. V. Dubonos, I. V. Grigorieva, and A. A. Firsov, Science **306**, 666 (2004).
[71] M. J. Allen, V. C. Tung, and R. B. Kaner, Chem. Rev. **110**, 132 (2010).
[72] S. K. Kannam, B. D. Todd, J. S. Hansen, and P. J. Daivis, J. Chem. Phys. **136**, 024705 (2012).
[73] T. Werder, J. H. Walther, R. L. Jaffe, T. Halicioglu, and P. Koumoutsakos, J. Phys. Chem. B **107**, 1345 (2003).
[74] T. A. Ho and A. Striolo, J. Chem. Phys. **138**, 054117 (2013).
[75] N. Asproulis and D. Drikakis, Phys. Rev. E **81**, 061503 (2010).
[76] N. Asproulis and D. Drikakis, Phys. Rev. E **84**, 031504 (2011).
[77] M. Darbandi, M. Sabouri, and S. Jafari, Numer. Heat Transfer, Part B **63**, 248 (2013).
[78] C. Liu and Z. Li, J. Chem. Phys. **132**, 024507 (2010).
[79] D. Wolf, P. Keblinski, S. R. Phillpot, and J. Eggebrecht, J. Chem. Phys. **110**, 8254 (1999).
[80] J. S. Hansen, T. B. Schroder, and J. C. Dyre, J. Phys. Chem. B **116**, 5738 (2012).
[81] P. A. Thompson and S. M. Troian, Nature (London) **389**, 360 (1997).
[82] S. Maruyama and T. Kimura, Therm. Sci. Eng. **7**, 63 (1999).
[83] T. Ohara and D. Suzuki, Microscale Thermophys. Eng. **4**, 189 (2000).
[84] J. Koplik, J. R. Banavar, and J. F. Willemsen, Phys. Fluids A **1**, 781 (1989).
[85] F.-Q. Song and J.-D. Wang, J. Hydrodyn. **22**, 513 (2010).
[86] S. Murada and I. K. Puri, Appl. Phys. Lett. **92**, 133105 (2008).
[87] L. Xue, P. Keblinski, S. R. Phillpot, S. U.-S. Choi, and J. A. Eastman, J. Chem. Phys. **118**, 337 (2003).
[88] B. D. Todd, P. J. Daivis, and D. J. Evans, Phys. Rev. E **51**, 4362 (1995).

[89]B. D. Todd and D. J. Evans, J. Chem. Phys. **103**, 9804 (1995).
[90]B. D. Todd, D. J. Evans, and P. J. Daivis, Phys. Rev. E **52**, 1627 (1995).
[91]C. Liu, H.-B. Fan, K. Zhang, M. M. F. Yuen, and Z. Li, J. Chem. Phys. **132**, 094703 (2010).
[92]Z. Ge, D. G. Cahill, and P. V. Braun, Phys. Rev. Lett. **96**, 186101 (2006).
[93]A. J. Schmidt, J. D. Alper, M. Chiesa, G. Chen, S. K. Das, and K. Hammad-Schifferli, J. Phys. Chem. C **112**, 13320 (2008).
[94]Z. Liang and H.-L. Tsai, Phys. Rev. E **83**, 061603 (2011).
[95]J. D. Weeks, D. Chandler, and H. C. Andersen, J. Chem. Phys. **54**, 5237 (1971).